Asymmetric double-layer charging in a cylindrical nanopore under closed confinement

Cite as: J. Chem. Phys. 152, 084103 (2020); https://doi.org/10.1063/1.5139541 Submitted: 20 November 2019 . Accepted: 04 February 2020 . Published Online: 24 February 2020

Mpumelelo Matse 📵, Peter Berg, and Michael Eikerling 🗓







ARTICLES YOU MAY BE INTERESTED IN

Interference of electrical double layers: Confinement effects on structure, dynamics, and screening of ionic liquids

The Journal of Chemical Physics 152, 074709 (2020); https://doi.org/10.1063/1.5144260

Microcanonical coarse-graining of the kinetic Ising model

The Journal of Chemical Physics 152, 084104 (2020); https://doi.org/10.1063/1.5139228

Gibbs free energy change of a discrete chemical reaction event

The Journal of Chemical Physics 152, 084116 (2020); https://doi.org/10.1063/1.5140980



Your Qubits. Measured.

Meet the next generation of quantum analyzers

- Readout for up to 64 gubits
- Operation at up to 8.5 GHz, mixer-calibration-free
- Signal optimization with minimal latency







Asymmetric double-layer charging in a cylindrical nanopore under closed confinement

Cite as: J. Chem. Phys. 152, 084103 (2020); doi: 10.1063/1.5139541 Submitted: 20 November 2019 • Accepted: 4 February 2020 • Published Online: 24 February 2020









Mpumelelo Matse, 1,a) Deter Berg, and Michael Eikerling 4 D



AFFILIATIONS

- Department of Physics, Simon Fraser University, Burnaby, British Columbia V5A 1S6, Canada
- ²Department of Science, University of Alberta, Camrose, Alberta T4V 2R3, Canada
- ³Department of Physics and Department of Chemistry, Simon Fraser University, Burnaby, British Columbia V5A 1S6, Canada
- FEK-13, Institute of Energy and Climate Research, Forschungszentrum Jülich GmbH, 52425 Jülich, Germany

ABSTRACT

This article presents a physical-mathematical treatment and numerical simulations of electric double layer charging in a closed, finite, and cylindrical nanopore of circular cross section, embedded in a polymeric host with charged walls and sealed at both ends by metal electrodes under an external voltage bias. Modified Poisson-Nernst-Planck equations were used to account for finite ion sizes, subject to an electroneutrality condition. The time evolution of the formation and relaxation of the double layers was explored. Moreover, equilibrium ion distributions and differential capacitance curves were investigated as functions of the pore surface charge density, electrolyte concentration, ion sizes, and pore size. Asymmetric properties of the differential capacitance curves reveal that the structure of the double layer near each electrode is controlled by the charge concentration along the pore surface and by charge asymmetry in the electrolyte. These results carry implications for accurately simulating cylindrical capacitors and electroactuators.

Published under license by AIP Publishing. https://doi.org/10.1063/1.5139541

I. INTRODUCTION

With the continued development of interfacial sciences, a large body of research activity has been aimed at understanding the formation of electric double-layers (EDLs) in an electrolyte when interaction forces and potentials exist between charged surfaces. The structure and properties of the electric double layer (EDL) determine the electrostatic and electrokinetic properties of electrified interfaces, playing an important role in diverse technological and bio-physiochemical applications involving, among others, capacitive energy storage and conversion, 1,2 stabilization of colloidal systems,^{3–6} biomolecular recovery in oil/water interfaces,⁷ control of ion transport through charged channels of biological membranes, 8-10 plasma treatment of surfaces, 11 scanning electrometer for electric double-layer operation, ¹² and dielectrophoresis. ¹³

The desire to understand the fundamental processes taking place at EDL interfaces continues to inspire the development of experimental methods and theoretical models. Following its proposal by von Helmholtz¹⁵ in 1853, the EDL phenomenon was

increasingly given theoretical consideration, pioneered by the classical works of Gouy¹⁶ in 1910 and Chapman¹⁷ in 1913. In the "Guoy-Chapman (GC)" picture, the ions (regarded as point-like particles/charges) are mobile in a solvent that is modeled as a continuum dielectric and are driven by the coupled influences of diffusion and electrostatic forces within the framework of the Poisson-Nernst-Planck (PNP) equations.

The negligence of ion sizes, ion-ion interactions, and the structure of the solvent, associated with the application of the Poisson-Boltzmann (PB) equation, however, is invalid for large surface charges and electric potentials. Specifically, high ionic concentrations introduce steric repulsion and additional correlations among ions due to over-crowding. Therefore, there has been a continuous endeavor toward the modification of PB and PNP models to aptly account for the effect of finite ion size in the electrolyte solution. Stern, in his acclaimed work, 18 entrenched the ion size effect in the EDL theory by taking into account a distance of the closest approach, whereby mobile ions are excluded from the first molecular layer close to the surface. Later studies within mean-field

^{a)}Author to whom correspondence should be addressed: mmatse@sfu.ca

approximations on the inclusion of steric effects were based, predominantly, on statistical mechanical considerations. ^{19,20} Typically, the two-dimensional (2D) lattice-gas formalism^{20,21} is adopted to model the statistical distribution function and derive the free energy in the mean field approximation from which size-modified PB and PNP equations are obtained. The first complete size-modified PB model was developed by Bikerman,²² who accounted for equal ion sizes by including an entropy term for solvent molecules in the free energy. Over the next several years, many researchers have worked on the reformulation of Bikerman's modified PB (mPB) model to handle specific ion size effects. Notable work has been reported by Wickie and Eigen, 24-26 Strating and Wiegel, 26,27 Borukhov et al., 19 Bohinc et al., 28,29 Kornyshev, 30 Kilic et al., 31,32 and Bazant et al.33

From a computational point of view, the Bikerman model remains popular due to its relative ease of implementation and qualitatively good agreement with experiments and molecular dynamics simulations.^{34,35} Owing to recent numerical studies^{36–42} grounded in Bikerman modeling, many interesting phenomena such as capacitance-voltage curves, confinement effects, lattice saturation, improvement of cross-stream diffusion, over-screening effects, and layering of ions near electrode surfaces are now reasonably well understood. A majority of these studies consider systems under open boundaries^{43,44} in which the electrolyte is presumed to be in thermodynamic equilibrium with an electrolyte reservoir, the so-called "semi-grand canonical ensemble." The most studied system is an electrolyte solution in contact with a planar electrode surface or between parallel-plates with a voltage applied between them. The apparent scarcity of studies concerning closed systems could be due to two main reasons: (1) The difficulty in numerically solving the resulting integro-differential-equations complicated by the inclusion of conservation constraints. (2) In practice, electrokinetic devices are usually connected to reservoirs. However, the closed confinement of electrolytes between charged walls can present additional effects potentially resulting in rich phenomena that are particularly important in nanoscale devices. Particularly, electric double-layer capacitors for electrical energy storage and electroactive polymer actuators for artificial muscles are closed systems whose performance is dictated by the underlying EDL

In the present study, we obtain and discuss the numerical results of double-layer charging in a closed cylindrical pore. Inner walls of the pore's cylindrical section are lined by surface charges, mimicking the charged walls of a nanoporous polymeric host material. A binary electrolyte solution is enclosed inside the pore to maintain electro-neutrality, and the pore ends are blocked by electrodes with a potential bias applied between them. The pore under consideration is a characteristic of proton-conducting cylindrical pores in polymer electrolyte membranes (PEMs). 45,46 The most commonly used PEM material is Nafion, which consists of a polymeric elastic backbone, lined by grafted side chains that are terminated with sulfonic acid head groups. 47 Viscoelastic PEMs can be used in the fabrication of electroactuators, 48-50 which is a key motivating factor for our study. While we focus on rigid nanopores in this contribution, an extension to flexible pores^{51,52} will be part of future

We use a continuum mean-field theory, based on the modified PNP and PB equations, and study the EDL formation and relaxation near boundaries. Differential capacitance data are presented and analyzed, with a focus on its dependence on the pore surface charge density, electrolyte concentration, ion size, and pore size. The numerical model was modified to also account for asymmetry in the charge valencies and ion sizes of each individual ionic species, as well as a non-uniform distribution of charges along the pore surface.

This paper is organized as follows: The physical-mathematical methodology will be presented in Sec. II, including a brief outline of the governing equations, a presentation of the electroneutrality condition imposed onto the system for self-consistency, and the description of the numerical method employed. Section III presents numerical results. Here, the dynamics of the double layer formation are presented first. This is followed by parametric studies of differential capacitance data. Finally, Sec. IV concludes this paper with a summary of the results.

II. METHODOLOGY

A. Schematics and assumptions

In what follows, we are concerned with a binary symmetric *z*:*z* electrolyte solution. The case of asymmetric ion charges will be considered in Sec. III D only. The electrolyte is confined inside a charged cylindrical polymeric pore of radius *R* and length *L* with electrodes attached at both ends; see Fig. 1 for a schematic illustration. The walls of the pore carry charged head groups, which we will model as a uniform distribution with surface charge density σ_p . The problem is two-dimensional, with coordinates in the radial (r) and axial (z) directions. Cylindrical coordinates are adopted, with the origin fixed at the center of the inner surface of the left electrode. An externally applied potential bias ΔV is introduced between the electrodes, with the right electrode sitting at a higher potential and located at z = L.

In the basic simplified variant, both cations and anions are assumed to be equi-sized hard spheres of constant diameter a. Steric ion-ion interactions are taken into account within a continuous dielectric medium approach with constant permittivity, while advection of the electrolyte is assumed negligible—a reasonable assumption for pores with small radius (1-2 nm). Isothermal conditions are assumed to prevail in the system. Ions can accumulate at the electrode surfaces but without ion insertion into the electrode. We denote the net accumulated ion charges on the left and right electrode as Q_L and Q_R , respectively.

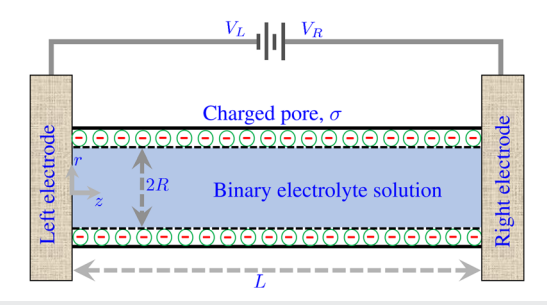


FIG. 1. Schematic illustration of the examined configuration: Electrolyte in a closed cylindrical pore in 2D cross section.

From a physical point of view, the model system presented above mimics closely confined and nearly cylindrical energy storage (e.g., capacitors and batteries) and generation devices or electroactuation devices. 48-50 We would like to emphasize that the highly confined ionic system studied in this work is expected to exhibit properties that are not accounted for in the Bikerman model. Because of this limitation, model results are expected to deviate from experimental findings. However, the goal here is to explore essential trends revealing the impact of core parameters on the double-layer capacitance. Other effects such as overscreening and the transition to crowding⁵³ are expected to play a role in regimes with high ion concentration. In addition, ion-wall interactions, ⁵⁴ correlations between water molecules, and image effects are expected to play a role. Such effects can be accounted for by employing molecular dynamics simulations of the system, which will be a subject of future work.

B. Governing equations

Following the Bikerman model, the free energy functional of the ionic system is modified, based on a mean-field approximation, by adding an ideal-gas-like solvent entropy term to account for overcrowding of ions and solvent molecules,

$$F = \int d^{3}r \left\{ -\frac{\varepsilon \varepsilon_{0}}{2} |\nabla \psi|^{2} + zq\psi(c_{+} - c_{-}) + k_{B}T \left[c_{+} \log(c_{+}a^{3}) + c_{-} \log(c_{-}a^{3}) \right] + k_{B}T \left[\frac{1 - a^{3}(c_{+} + c_{-})}{a^{3}} \log \left[1 - a^{3}(c_{+} + c_{-}) \right] \right) \right] \right\},$$
 (1)

where ψ is the electrostatic potential; c_{\pm} denotes the local concentration of negative and positive ionic species; k_B is the Boltzmann constant; ε_0 is the permittivity of free space; ε is the dielectric constant of the electrolyte; and T is the absolute temperature. The first two terms of the integral in Eq. (1) can be interpreted as the total electrostatic free energy. The first term is the dielectric self-energy of the electric field $E = -\nabla \psi$, and the second term gives the electrostatic energy of mobile ions. The remaining two terms represent entropic contributions of ions and solvent molecules, respectively. These terms penalize large ionic concentrations by imposing a cutoff on the value of ionic concentration, $c_{\pm}^{\text{max}} = 2^{1/2}/a^3$, which is the maximum density of close-packed (face-centered cubic or hexagonal close-packed) spheres of diameter a.

Demanding the variation of F with respect to c_{\pm} to be equal to the electrochemical potential μ_{\pm} of ionic species and the variation of F with respect to ψ to be zero, one obtains

$$\mu_{\pm} = \pm zq\psi + k_B T \log \left[\frac{c_{\pm} a^3}{1 - a^3 (c_+ + c_-)} \right]$$
 (2)

and the Poisson equation

$$\nabla \cdot (\varepsilon \varepsilon_0 \nabla \psi) = zq(c_+ - c_-), \tag{3}$$

respectively. Assuming that the diffusivities D for each ionic species are the same and constant, the modified Nernst-Planck equations for ionic fluxes are

$$J_{\pm} = -\frac{D}{k_B T} c_{\pm} \nabla \mu_{\pm}$$

$$= -D \nabla c_{\pm} \mp \frac{Dzq}{k_B T} c_{\pm} \nabla \psi + a^3 D \frac{c_{\pm} \nabla (c_{+} + c_{-})}{1 - a^3 (c_{+} + c_{-})}$$
(4)

and the conservation equations for the ionic species take the form

$$\frac{\partial c_{\pm}}{\partial t} + \nabla \cdot \boldsymbol{J}_{\pm} = 0. \tag{5}$$

At equilibrium, no ionic and fluid flows are present, i.e., $I_{+} = 0$. Using Eq. (4) and integrating $I_{+} = 0$ from some reference concentration c_0 gives the ionic concentrations (number density) in terms of the electric potential,

$$c_{\pm} = \frac{c_0 \exp\left(\frac{\mp zq\psi}{k_B T}\right)}{1 + 2(z+1)c_0 a^3 \sinh^2\left(\frac{zq\psi}{k_B T}\right)}.$$
 (6)

In this context, $c_0 = c_{\pm}(\psi = 0)$ is the reference concentration of both cations and anions at which the electric potential is set to be zero. Note that the region where $c_{\pm} = c_0$ does not need to be defined within the system. Substituting Eq. (6) into Eq. (3) gives the modified PB equation for the local steady-state electric potential in the electrolyte

$$\nabla \cdot (\varepsilon \varepsilon_0 \nabla \psi) = \frac{2zqc_0 \sinh\left(\frac{zq\psi}{k_B T}\right)}{1 + 2(z+1)c_0 a^3 \sinh^2\left(\frac{zq\psi}{k_B T}\right)}.$$
 (7)

C. Boundary conditions and electroneutrality

Having established the equations that model the dynamics and steady-state equilibrium for electrochemical properties of the system, we turn to the task of identifying all boundary conditions. All equations in Sec. II B are valid in the inner cylinder's volumetric domain Ω $(r \in [0, R], \theta \in [0, 2\pi], z \in [0, L])$, which is bounded by the cylindrical pore ∂_p $(r = R, \theta \in [0, 2\pi], z \in [0, L])$, left electrode ∂_L $(r \in [0, R], \theta \in [0, 2\pi], z = 0)$, and right electrode $\partial_R (r \in [0, R], \theta \in [0, 2\pi], z = L).$

The boundary conditions at the pore's inner walls are determined by the surface charge density and a vanishing electric field outside the pore,

$$\left(\varepsilon\varepsilon_0\nabla\psi\cdot\hat{\boldsymbol{n}}\right)\Big|_{\partial_p}=\sigma_p. \tag{8}$$

Here, \hat{n} is a unit vector normal to boundaries. At the pore surface, we do not consider any chemical reaction involving ions or functional

As a side note, the smaller the ratio between the dielectric constants of pore walls and the electrolyte, the lesser the degree to which the field will extend into the surrounding wall region. Strictly speaking, Eq. (8) is only valid in the limit of that ratio tending to zero, but it is an on-going debate as to how to assess the violation of Eq. (8) for small but non-zero ratios.

A central aspect of the model is the boundary condition for the electrostatic potential bias between the metal electrodes, which

is introduced externally. It can be expressed by

$$\psi|_{\partial_R} = V_R \quad \text{and} \quad \psi|_{\partial_L} = V_L.$$
 (9)

Each electrode surface, free of adsorbed species and charge transfer reactions, is taken to be ideally polarizable and its apparently nonuniform surface charge density is an unknown quantity, which can be controlled by adjusting the potential bias $\Delta V = V_R - V_L$ or the concentration of the electrolyte solution.

Conditions (8) and (9) are sufficient to numerically solve Eq. (7) for the potential and ion density distribution at equilibrium. If the boundary conditions for the modified PB problem are not chosen carefully, however, global electroneutrality (GEN) will generally be violated, which is unphysical for a closed system that must retain the electroneutrality of its initial (reference) state. We define a reference state with uncharged electrodes, $Q_L = Q_R = 0$ for which $\Delta V = 0$, corresponding to the potential (or, better, voltage) of zero charge (PZC) of the capacitor configuration. In this state, an exact charge balance is fulfilled between the net ionic charge in the electrolyte solution and the fixed surface charge on the polymeric pore surface, which is given by

$$zq \int_{\Omega} d^3 \mathbf{r} (c_+ - c_-) + \int_{\partial_0} d^2 \mathbf{r} (\varepsilon \varepsilon_0 \nabla \psi \cdot \hat{\mathbf{n}}) = 0, \tag{10}$$

and this is referred to as the global electroneutrality (GEN) in the context of our study. In the case with charged electrodes, we control the metal-phase potential at one of the electrode interfaces, tacitly assumed to be uniform, relative to the potential of zero charge. Then, the metal phase potential of the second electrode cannot be known a priori but needs to be chosen self-consistently so as to uphold the condition of global electroneutrality. In addition to (9), the following balance condition must be fulfilled in the charged

$$Q_L + Q_R = \int_{\partial_I} d^2 \mathbf{r} (\varepsilon \varepsilon_0 \nabla \psi \cdot \hat{\mathbf{n}}) + \int_{\partial_R} d^2 \mathbf{r} (\varepsilon \varepsilon_0 \nabla \psi \cdot \hat{\mathbf{n}}) = 0, \quad (11)$$

where the total charges on left and right electrodes, Q_L and Q_R , are defined through the respective integrals. In essence, the metal phase potential at one electrode is treated as a free parameter. For numerical calculations reported herein, V_R is provided and a potential range must be scanned until the unique value of V_L is found so that condition (11) holds for a given value of c_0 . These conditions are sufficient to find a unique and physically consistent solution of the problem. Thus, the output of numerical calculations includes the total voltage difference and amount of charge that is being shifted between the electrodes.

D. Constitutive relations and numerical methods

The present study focuses on aqueous binary and monovalent (symmetric) electrolyte solutions at room temperature, with the basic set of parameters listed in Table I. Equations (5) and (7), along with the boundary conditions given by Eqs. (8)-(11), are solved using the commercial finite element solver COMSOL 5.4. To reduce computational cost, only a single 2D domain of the rotationally symmetric model is considered. This is realized in COMSOL by choosing the "2D axisymmetric" component. The "general form PDE" mode

TABLE I. Parameters of the system.

Parameter	Description	Reference value
9	Elementary charge	1.602 · 10 ⁻¹⁹ C
k_B	Boltzmann constant	$1.38 \cdot 10^{-23} \text{ J/K}$
ϵ_0	Vacuum permittivity	$8.85 \cdot 10^{-12} \text{ F/m}$
ϵ	Dielectric constant	80
T	Temperature	300 K
D	Ion diffusivity	$1 \cdot 10^{-5} \text{ cm}^2/\text{s}$
R	Pore radius	2 nm
L	Pore length	10 nm
L	Pore length	10 ni

and electrostatics module are used to solve for the time-dependent PNP and the stationary PB problem, respectively.

The computational domain $(R \times L = 2 \text{ nm} \times 10 \text{ nm})$ is discretized into quadratic triangular elements. Nonuniform elements are employed with a finer mesh generated near boundaries to capture the EDLs. Typically, the applied triangular mesh comprises mesh elements with dimensions ranging from about 0.03 Å in the vicinity of the electrodes and pore interfaces to about 0.1 Å at the center of the domain. The numerical model includes about 10 000 mesh elements and 20 000 degrees of freedom. COMSOL's numerical scheme has been validated to be adequately accurate for solving comparable electrokinetic problems, and a comprehensive description of its numerical implementation is accessible in the literature.⁵⁶ Convergence and mesh-independence of all results are verified first.

III. RESULTS AND DISCUSSION

A. Time evolution of double layers

Steady-state equilibrium solutions are the main focus in the literature for comparable problems, chiefly for the EDL structure and capacitance studies. In this work, the preliminary step is to investigate the non-equilibrium dynamics aspects. In particular, we examine the temporal evolution of the electric potential and ion density distribution across the entire domain. Our own interest in exploring the system's non-equilibrium dynamics stems from two key motivations: (1) Understanding the formation and relaxation of EDLs is critically important for practical applications such as controlling the performance of electrochemical devices such as supercapacitors. (2) The second motivation, detailed below, is that numerical simulations of the dynamics will provide useful insight into the interconnection between the dynamical model described by the modified PNP equations and the equilibrium model characterized by the modified PB equation satisfying the electroneutrality condition in Eq. (11).

In Sec. II C, we highlighted that for a given set of conditions, there is a unique potential difference between the electrodes that ensures electroneutrality. For numerical solutions at equilibrium via the modified PB equation, this ΔV is essentially the output of the model. For solving the dynamics via the modified PNP-based numerical solver, however, it is necessary that ΔV is predetermined initially. Our general strategy to ensure that the dynamics is driven to

a globally electroneutral equilibrium state involves an initial equilibration of the system before studying its dynamics. In this approach, we begin with the task of solving for the equilibrium problem by appealing to the modified PB equation, given a set of conditions such as σ_D and the net amount of charge enclosed in the volume, dictated by c_0 . From the results of the mPB solver, ΔV is extracted to be used as the Dirichlet boundary condition for the dynamical model. The second step is to solve the full modified PNP equations, assuming no fluxes at all boundaries, along with boundary conditions in Eqs. (8) and (9). The dynamics starts off with an electroneutral state. For simplicity, a uniform density of cations and anions, i.e., c_{\pm}^{initial} , is given as an initial condition at t = 0. The value of c_0 used in the equilibration step places a powerful constraint on the choice of $c_{\pm}^{\rm initial}$. Although this choice of $c_{\pm}^{\rm initial}$ seems unphysical, it helps understand a typical nonequilibrium response of ions in the channel to both the surface charges and the electrode potential bias. To understand this idea more concretely, the link between c_0 and $c_+^{initial}$ needs to be addressed.

Within the modified PB solver, σ_p determines the net amount of charge, $Q_{\rm net}$, due to electrolyte ions in the volumetric domain and c_0 determines the total amount of positive and negative ionic charges $(Q_+$ and $Q_-)$ enclosed as follows:

$$Q_{\text{net}} = -\int_{\partial_p} d^2 \mathbf{r} \, \sigma_p \tag{12}$$

and

$$Q_{\pm} = \pm \int_{\Omega} d^3 \mathbf{r} \, \frac{q c_0 \exp\left(\frac{\mp z q \psi}{k_B T}\right)}{1 + 2(z+1)c_0 a^3 \sinh^2\left(\frac{z q \psi}{k_B T}\right)},\tag{13}$$

where $Q_{\rm net}=Q_++Q_-$ must be fulfilled—the condition of global electroneutrality. In light of this, it is straightforward that the initial condition $c_\pm^{\rm initial}=Q_\pm/q\pi R^2 L$ will lead to a consistent solution for the dynamics when charge conservation is enforced in the modified PNP solver. The system is then driven accordingly from this non-equilibrium state to an equilibrium state, whose solutions converge to those of the modified PB solver.

In COMSOL, the modified PB solver is executed by solving Eq. (7) using the "charge conservation" model builder under the "AC/DC-electrostatics" module. Equation (11) is implemented via the "floating potential" function. The modified PNP-based solver, however, introduces time dependence by additionally solving Eq. (5) using the "general form PDE" solver under the "mathematics-PDE interface" module.

Figure 2 shows a 2D representation of the time evolution of the EDL in a pore, whose polymetric walls are negatively charged $(\sigma_p = -0.1 \text{ C/m}^2)$ and to which a potential bias $\Delta V = 0.121 \text{ V}$, obtained from the mPB solver, is applied at t = 0. The underlying color shows the local cation concentration, white contours represent the electric potential, and arrows give the cation flux density vector field. In a more compact way of illustrating the ion dynamics in the pore, Fig. 3(a) shows the total ion concentration, $c_t = c_+ + c_-$, along the center of the pore (r = 0) at different times and Fig. 3(b) shows the charge on each electrode, Q_L and Q_R , as a function of time in the range 1–20 ns.

By virtue of these results, we distinguish four regimes in the relaxation dynamics: at very short times, Fig. 2 shows a sudden

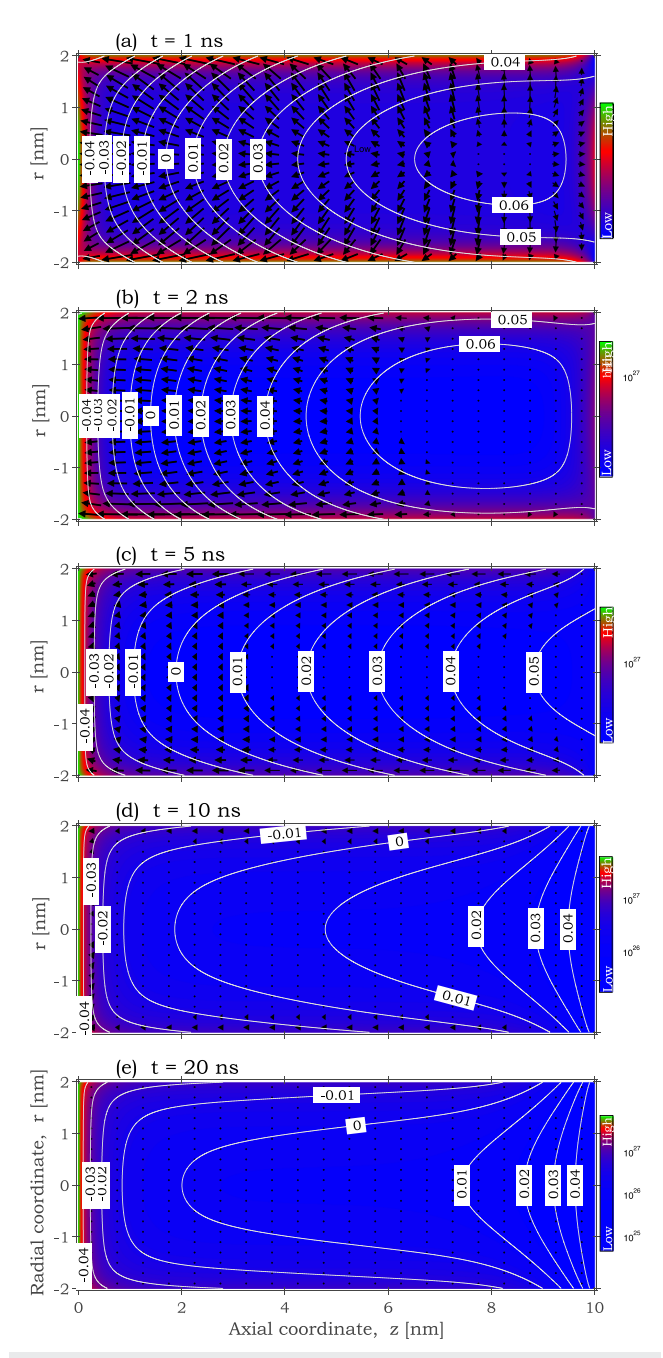
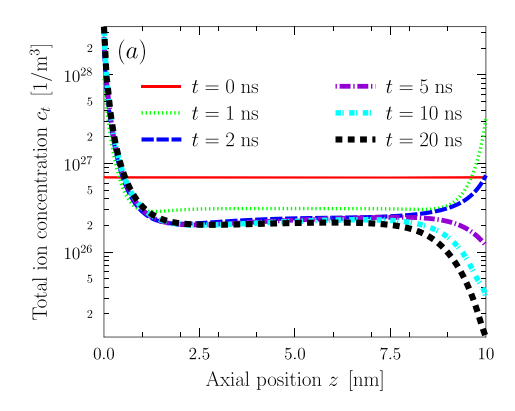


FIG. 2. Two-dimensional view of the time evolution and relaxation of the EDL at (a) t=1 ns, (b) t=2 ns, (c) t=5 ns, (d) t=10 ns, and (e) t=20 ns. The image plot gives the concentration of cations c_+ , contour plots represent the electric potential ψ , and the arrows give the flux density vector for positive ions J_+ . Parameter values: z=1, $\sigma_p=-0.1$ C/m², $\Delta V=0.121$ V, and $c_0=0.02$ M.

displacement of counterions (cations) toward all boundaries. This corresponds to a time regime far out of equilibrium. The system is forced to balance strong local electric fields that develop from it, being initially set to be extremely out of equilibrium. Here, all



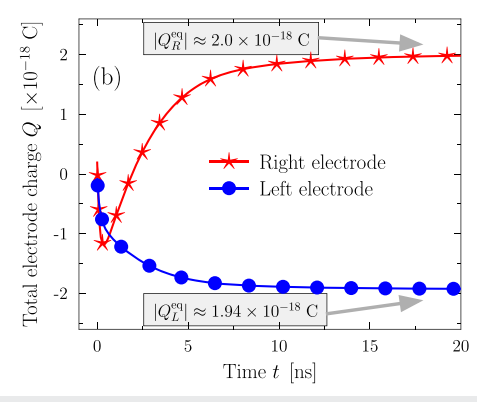


FIG. 3. (a) Variation of the total ion concentration, $c_t = c_+ + c_-$, along the center of the pore. (b) Variation of total charge on left and right electrodes, viz., Q_L and Q_R , as a function of time. Parameters are z = 1, $\sigma_p = -0.1$ C/m², $\Delta V = 0.121$ V, and $c_0 = 0.02M$

boundaries become negatively charged. This effect manifests itself as the rapid dip in the blue curve in Fig. 3(b). In the next time regime, anions accumulate at the right electrode (sitting at a higher potential) and counterions (cations) are translated toward the negative electrode. This is observed in Fig. 2 at t = 5 ns. The lateral diffusion of counterions in the first layer near the pore walls is actually faster than that in the bulk. The next time regime, which occurs on a much longer time scale, is the "EDL relaxation" phase. In this regime, seen at t = 10 ns in Fig. 2, there is no diffusion of counterions in the bulk. However, we observe a small-scale translation of counterions in the EDL largely due to the slow ion diffusion involved during EDL reorganization. The final time regime corresponds to a steady-state equilibrium. This is characterized by the plateaus of both curves in Fig. 3(b), approached at around t = 20 ns. It is imperative that the results in this regime agree with those from the modified PB solver, i.e., electroneutrality must be fulfilled. According to Fig. 3(b), the values of Q_R^{eq} and Q_L^{eq} are 2 × 10⁻¹⁸ C and 1.94×10^{-18} C, respectively, exhibiting a deviation of no more than 3%. Hence, we can confidently say that, through using the modified PNP model and a careful choice of initial conditions, we are able to drive the system from some non-equilibrium state to an equilibrium state that satisfies both condition (11) and the modified PB equation.

B. Differential capacitance

The voltage-dependent capacitance of the EDL is a parameter that plays a significant role in the characterization of the EDL structure in electrochemical systems. Of key interest in experimental studies is the differential capacitance, C_{diff} , defined as

$$C_{\text{diff}} = \frac{1}{\pi R^2} \frac{\partial Q_{\text{R}}^{\text{eq}}}{\partial \Delta V}, \tag{14}$$

where the total charge at the right electrode

$$Q_{\rm R}^{\rm eq} = \int_{\partial_{\rm R}} {\rm d}^2 \mathbf{r} \left(\varepsilon \varepsilon_0 \frac{\partial \psi}{\partial z} \right) \tag{15}$$

is evaluated at equilibrium. In essence, Cdiff represents the ability of an electrochemical cell to store charge at its electrodes in response to a perturbation potential applied between them. Capacitance data provide an important indirect means to assess the EDL structure since the local charge imbalance occurs only in the EDL region.

When calculating the differential capacitance, the total amount of individual positive and negative charges enclosed in the pore is conserved. We define the total ion number enclosed in ∂V as

$$N_{\text{ion}} = \frac{1}{a} (|Q_{+}| + |Q_{-}|) = \int_{\partial V} (c_{+} + c_{-}) d^{3} \mathbf{r}.$$
 (16)

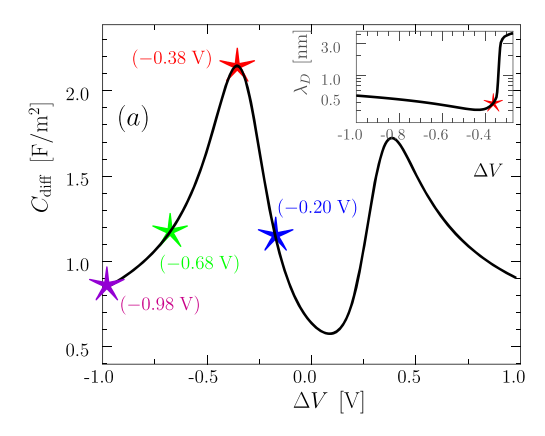
We require that N_{ion} stays constant as we probe through ΔV . This is achieved by setting the constraint (16) for some constant N_{ion} while ΔV is adjusted, via changing V_R , so that Eq. (11) is fulfilled. The "global constraints" function in COMSOL enforces this condition. In this work, C_{diff} curves are computed as follows: The total charge at each voltage is calculated via Eq. (15). The derivative in Eq. (14) is then computed numerically for ascending values of ΔV . About 100 data points (voltages) are used for each curve.

Figure 4(a) shows a typical plot of C_{diff} as a function of ΔV . Two noteworthy features of the C_{diff} curve are apparent: (1) the presence of a double peak and (2) the lack of symmetry with respect to ΔV . The former is attributed to excluded-volume-interaction-effects. We show and discuss Fig. 4(b) to support this view. Foremost, we formalize the discussion by defining the cross-sectionally averaged total ion density with respect to the axial distance from the left electrode,

$$\bar{c}_{t}(z) = \frac{2}{R^{2}} \int_{0}^{R} c_{t}(r, z) r dr.$$
 (17)

This quantity, compared to taking c_t along the center of the pore, provides a more rigorous measure of the axial ion density profile in 1D due to the strong radial variations of *c* when the pore is strongly

Figure 4(b) shows plots of $\bar{c}_t(z)$ for a few values of ΔV around, and inclusive of, the left peak in Fig. 4(a). Four colored markers in Fig. 4(a) correspond to the colored distributions shown in Fig. 4(b). On account of these results, we understand that the decline of C_{diff} at high positive or negative ΔV appears to be a consequence of overcrowding of counterions near the electrodes: at higher $|\Delta V|$, \bar{c}_t increases at a faster rate near the electrode surface and the decay length (λ_D) of $\bar{c}_t(z)$ decreases sharply. [Here, the decay length is defined as the distance from the left electrode at which $\bar{c}_t(z)$ is reduced to 1/e of its peak value attained directly at the electrode



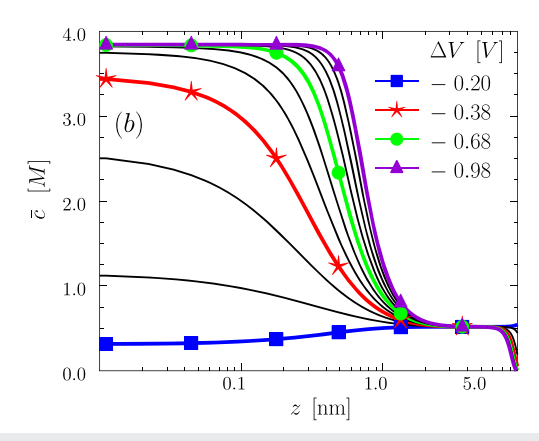


FIG. 4. (a) Variation of $C_{\rm diff}$ with ΔV . (b) Cross-sectionally averaged total ion concentration, $\bar{c}_{\rm t}(z)$, as a function of distance from the left electrode. Parameter values: z = 1, σ_p = -0.1 C/m², a = 3 Å, c_0 = 0.02M, and $N_{\rm ion}$ = 135.91.

surface.] This behavior is observed up to the peak voltage, indicated by the red curve in Fig. 4(b). Beyond the peak, counterions saturate near the electrode and can only further accumulate by growing the thickness of the saturation layer to distances further away from the surface. This leads to a sudden change in λ_D as a function of ΔV , as shown in the inset of Fig. 4(a), caused by ion screening.

The lack of symmetry in $C_{\rm diff}$ in Fig. 4(a) is attributed to the presence of fixed charges on the pore wall. This effect is demonstrated in Fig. 5, where $Q_{\rm R}^{\rm eq}$ is plotted against ΔV at different values of σ_p . We recognize the existence of symmetry only when the pore is uncharged, i.e., at $\sigma_p=0$. When the pore is charged, reversing the sign of ΔV leads to a different magnitude of net charge on each electrode. This can be ascribed to the global electroneutrality condition enforced in the system: consider the pore with $\sigma_p<0$ and the right electrode at a negative potential with respect to the left electrode; by electroneutrality, there are more cations (majority charge carriers) than anions (minority charge carriers) in Ω ; in this case, $C_{\rm diff}$ arises primarily from the large amount of cations in the pore, giving a high $Q_{\rm R}^{\rm eq}$. If the right electrode is at a positive potential, the low amounts of negative charged co-ions (minority charge carriers

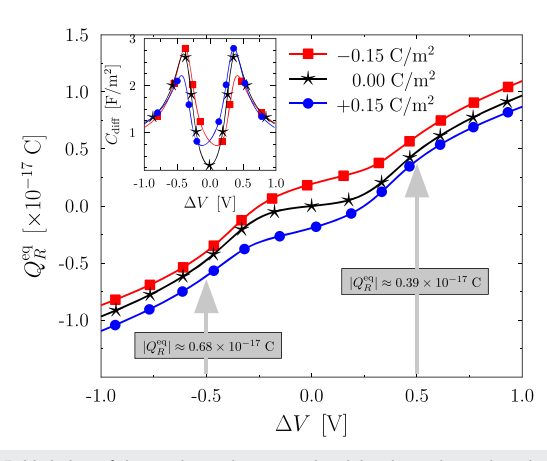


FIG. 5. Variation of the total net charge on the right electrode against the electrode potential bias ΔV to illustrate the lack of symmetry in differential capacitance curves (the inset shows the corresponding differential capacitance curves). Parameter values: z = 1, $c_0 = 0.02$ M, a = 3 Å, and $N_{\text{ion}} = 135.91$.

in the pore) are drawn toward this electrode, resulting in a relatively diminished $|Q_{\rm R}^{\rm eq}|.$

Figure 6 shows the effect of σ_p on the potential (or voltage) of zero charge (PZC), i.e., the point at which $|Q_{\rm R}^{\rm eq}|=0$. As a consequence of the previously explained asymmetry, the PZC is shifted relative to ΔV , with the sign and magnitude of this shift exhibiting a dependence on σ_p : the more negative the σ_p , the more negative the value of ΔV at which $|Q_{\rm R}^{\rm eq}|=0$. This figure, thus, embodies in a highly condensed form the consequence of using a charged porous host matrix, such as that provided by a polymer electrolyte membrane, for energy storage in double-layer capacitive devices. The inset of Fig. 6 shows the symmetry parameter $\alpha = C_{\rm diff}^{\rm peak, \ left}/C_{\rm diff}^{\rm peak, \ right}$

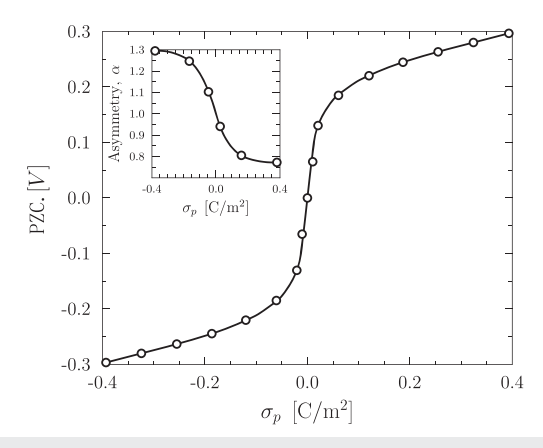
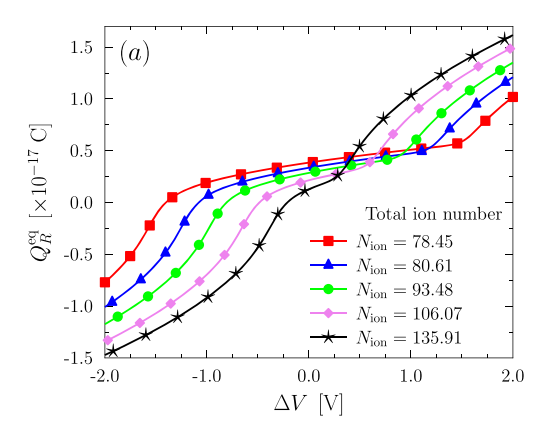


FIG. 6. The influence of surface charge density on the point of zero charge on the right electrode (the inset shows the ratio of the voltage peak on the left to that on the right in the DC curve). Parameter values: z = 1, $c_0 = 0.02$ M, a = 3 Å, and $N_{\rm ion} = 135.91$.

which is the ratio of the left peak differential capacitance to the right one.

The effect of $N_{\rm ion}$ on the electrode charging is illustrated in Fig. 7. At low $N_{\rm ion}$, the electrode charging is insensitive to changes in low ΔV and only high ΔV can lead to EDL overcrowding, forcing the peaks in $C_{\rm diff}$ to be farther apart and, thus, widening the low-capacitive plateau. At high $N_{\rm ion}$, however, the peaks move closer together, owing to ion saturation, and the local central minimum of $C_{\rm diff}$ increases. This agrees with similar studies in the literature, ⁵⁷ albeit for different geometries, where it is observed that, at even higher $N_{\rm ion}$, the $C_{\rm diff}$ curve transitions to just a single peak. For the case of a closed cylinder, simulations do not allow for such high concentrations required to see a single peak.

Figure 8 shows the effects of a on $C_{\rm diff}$. Here, we note that a shifts the voltage bias at peak $C_{\rm diff}$ ($\Delta V_{\rm peak}$) without affecting the results at small $|\Delta V|$. This underlines the excluded-volume-interaction effects seen only at high $|\Delta V|$ and the reduction to the Gouy–Chapman regime at low $|\Delta V|$. Predictably, a large a enhances the overcrowding effect of counterions as the competition for volume becomes fiercer. Hence, peaks in $C_{\rm diff}$ occur at lower $|\Delta V|$.



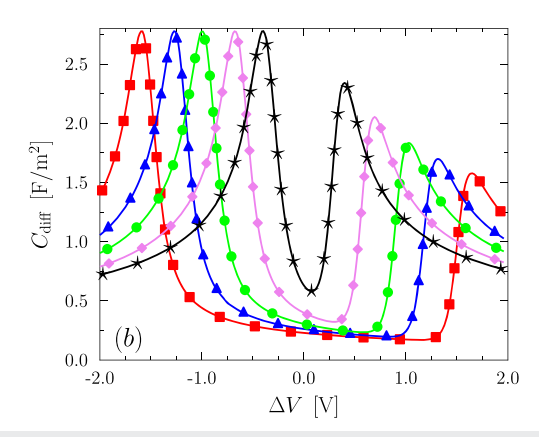


FIG. 7. The influence of $N_{\rm ion}$ on (a) the total amount of charge on the right electrode and (b) the differential capacitance as a function of the voltage bias. Parameter values: z = 1, $\sigma_p = -0.1$ C/m², and a = 3 Å.

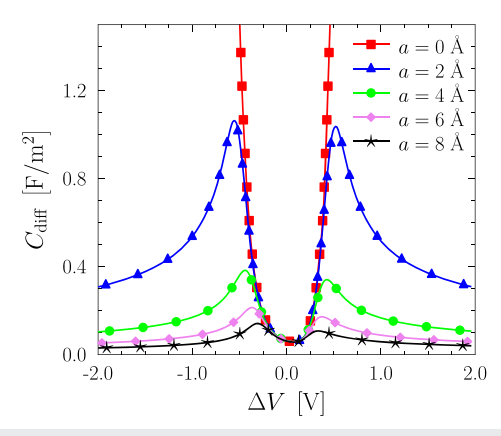


FIG. 8. Variation of the differential capacitance with the electrode potential bias at different values of a and R. Reference parameter values: z = 1, $\sigma_p = -0.1$ C/m², a = 4 Å, $c_0 = 0.02$ M, R = 10 nm, and $N_{\rm ion} = 135.91$.

C. Effect of asymmetry on ion properties

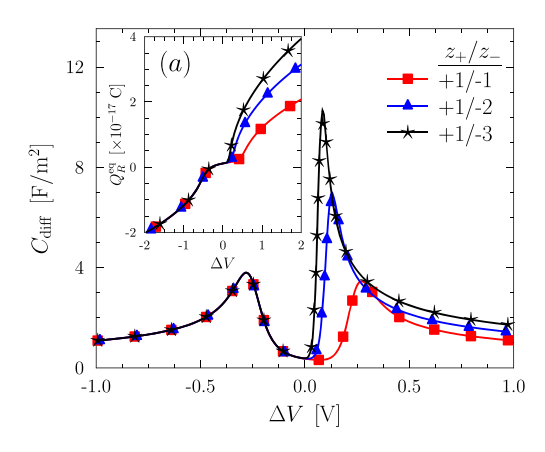
So far, we have considered electrolytes having two ionic species with identical valency and size. However, experimental data reported on capacitors in the literature ^{58–60} utilize electrolytes with an asymmetric valence. In addition, asymmetric electrolytes have practical implications in capacitive deionization ⁶¹ and biosensors. ⁶²

We now investigate the impacts of asymmetry on the electrolyte valency within the modified PB description. For nonidentical valency and ionic sizes, a complete rederivation based on the formalism presented in Sec. II B gives the modified Boltzmann distributions of cations and anions, 63

$$c_{\pm} = \frac{c_0 e^{\mp \frac{z_{\pm} q \psi}{k_B T}}}{1 + c_0 a_+^3 \left(e^{-\frac{z_{\pm} q \psi}{k_B T}} - 1 \right) + c_0 a_-^3 \left(e^{-\frac{z_{\pm} q \psi}{k_B T}} - 1 \right)},$$
(18)

where z_{\pm} and a_{\pm} denote the valency and ion size, respectively, for cations and anions.

Differential capacitance results are shown in Fig. 9. In Fig. 9(a), the valency of anions is varied. We see a pronounced asymmetry in C_{diff} curves as a manifestation of the asymmetry in ionic valency. Asymmetry in the double layer structure originates from an imbalance between the magnitude of forces experienced by cations and anions, dictated by the ionic valence. The effect of z_+/z_- is only seen at positive ΔV since the valency of positive ions, which controls the DC curve when $\Delta V < 0$, is fixed here. Another key observation is that the position of a local maximum shifts toward lower ΔV when the ionic asymmetry increases. This observation is consistent with the prediction that high valency leads to a stronger electric force and, hence, a stronger ion saturation effect. Figure 9(b) shows a similar effect when ion sizes are asymmetric. Changing a_+ only affects the left hump of the $C_{
m diff}$ curve and a_- affects the right hump. These results highlight feasible exploitations of valence asymmetry as a way to tune the energy and power density of capacitors.



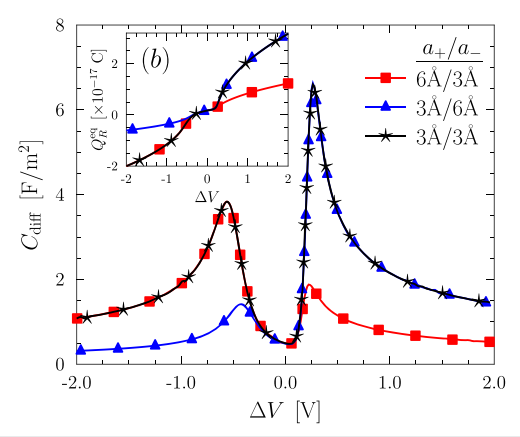


FIG. 9. Differential capacitance against the electrode potential bias at various values of (a) z_+/z_- and (b) a_+/a_- . The insets show the amount of net charge on the right electrode. Graph (b) uses asymmetric valences $z_+/z_- = + 1/-2$. Parameter values: $\sigma_p = -0.05 \, \text{C/m}^2$, $c_0 = 0.02 \, \text{M}$, $a = 4 \, \text{Å}$, and $N_{\text{ion}} = 97.3$.

The sectional ion density profiles along the pore at different values of z_+/z_- are shown in Fig. 10. Both cation and anion profiles are affected. The more pronounced saturation of cations near the left electrode is observed at larger z_- , while their distribution away from the left electrode is unaffected. The anion distribution, however, is affected throughout the length of the pore. We see a stronger pull of anions toward the left electrode at higher z_- .

D. Effect of surface charge density modulation

We saw in Sec. III B that the presence of a uniform charge density distribution on the pore surface introduces asymmetry in $C_{\rm diff}$ curves and offers a way of modifying the double-layer structure near each electrode. In this section, we investigate the effect of a non-uniform distribution of σ_p .

First, we consider a $\sigma_p(z)$ profile that follows a cyclic square-wave-like modulation defined in the following manner: let n_{σ} be the (even) number of equal segments along the length of the pore with a constant surface charge density that switches between $-\sigma_0$ and σ_0 .

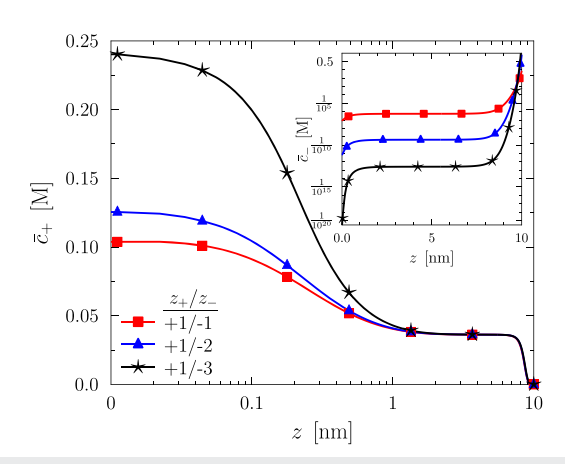


FIG. 10. Cross-sectional concentration of cations. The inset shows the cross-sectional concentration of anions. Parameter values: $\sigma_p = -0.05 \text{ C/m}^2$, $c_0 = 0.02\text{M}$, and a = 4 Å.

Mathematically, this can be expressed by

$$\sigma_p(z) = \begin{cases} -\sigma_0 & \text{for } \frac{2kL}{n_\sigma} \le z < \frac{(2k+1)L}{n_\sigma} \\ +\sigma_0 & \text{for } \frac{(2k+1)L}{n} \le z < \frac{2kL}{n}, \end{cases}$$
(19)

where $k=0, 1, 2, \ldots, n_{\sigma}/2$, with n_{σ} being even. With this profile, the net amount of charge on the pore surface is zero. We use $\sigma_0 > 0$ so that the negatively charged left electrode is closer to a negative section of the pore.

The case $n_{\sigma}=2$ is of particular relevance as it corresponds to the case of nanofluidic diodes. Wherever, this pore configuration mimics the interfacial conditions encountered in electrochemical devices with bipolar membranes, 66-68 where a contact region between a proton exchange membrane (PEM) and an anion exchange membrane (AEM) exists. In the latter context, it is of foremost interest to determine the potential distribution and corresponding electric field strength in the junction or space charge region where the two ion-conducting media with different majority carriers meet, carrying major implications in a wide array of systems including fuel cells, electrolyzers, electrodialysis, capacitive electrodes, and colloidal systems.

Figure 11 shows results for a 2D slice of the pore along the axial direction for the case $n_{\sigma}=2$ for different values of σ_0 . Colored images show the net ion concentration $c_{\rm net}=c_+-c_-$, and labeled contours illustrate the electric potential in volts. As expected, counterions are drawn toward oppositely charged sections of the pore. We observe a formation of an electric field across the junction region. The variation of the axial electric field with σ_0 along the center of the pore (r=0) is shown in Fig. 12. We note that the strength of the local electric field in the space charge region reaches values of 10^8 V/m, within a region of about 5 nm wide. At large $|\sigma_0|$, the junction region gets narrower and the associated electric field in the region increases in strength. These results agree qualitatively with Ref. 67, where the modeling is based on PNP equations and fixed ionomer charges are

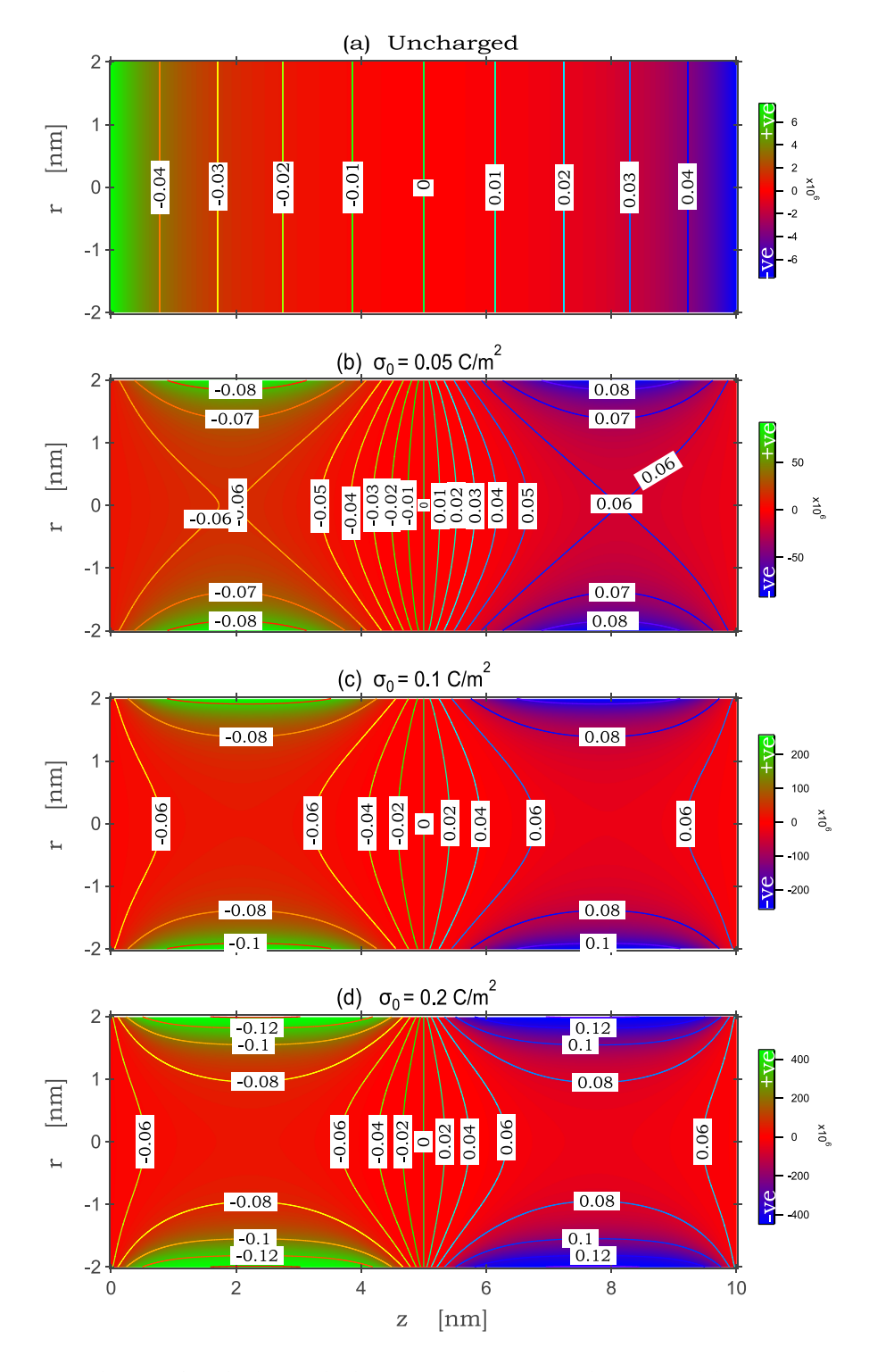


FIG. 11. Effect of σ_0 on charge distribution within the pore for the case $n_\sigma=2$ at the following surface charge densities: (a) $\sigma_0=0$ C/m² (uncharged), (b) $\sigma_0=0.05$ C/m², (c) $\sigma_0=0.1$ C/m², and (d) $\sigma_0=0.2$ C/m². Distribution of net ion concentration (color plot) and the electric potential (contour plots with labels in volts) on a 2D slice along the pore. Parameter values: z=1, $c_0=0.02$ M, and a=6 Å.

treated as a uniform background. The net ion concentrations along the center of the pore are shown in the inset of Fig. 12, and the results indicate ion depletion at the bipolar junction region and near the electrodes. This arises from Coulombic interactions between the

mobile ionic species within the space charge region and the fixed ionic charges at the pore walls and electrodes. Lower $|\sigma_0|$ reduces the electric field at the junction region and forms a less compact space charge region.

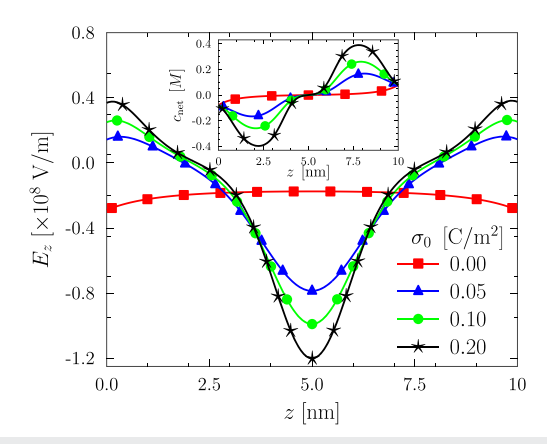


FIG. 12. Net ion concentration along the center of the pore for different values of σ_0 . The inset shows the corresponding axial electric field ($E_z=-\psi_z$). Parameter values: z=1, $c_0=0.02M$, and a=6 Å.

IV. CONCLUSIONS

This paper presented numerical simulations of electric double layers formed by a binary electrolyte in a closed, cylindrical, and charged nanopore whose ends are met by metal electrodes, subject to an externally applied potential bias. The applied model consists of the modified Poisson-Nernst-Planck/Poisson-Boltzmann equations, accounting for finite-ion sizes similar to the Bikerman model. A self-consistent electroneutrality condition at equilibrium was enforced that requires equal magnitudes of net charges on the electrodes. Application of this condition establishes the correct correspondence between the modified Poisson-Nernst-Planck and Poisson-Boltzmann equations at equilibrium. Numerical results were presented that illustrate the formation and relaxation of double-layer charging near the electrodes and the internal pore surface. Differential capacitance data were analyzed and discussed, with a focus on their dependence on the pore surface charge density, electrolyte concentration, ion sizes, and pore size. The results indicate that the structure of the double layer near the electrode can be controlled or is affected by the charge distribution along the pore, the asymmetry in the total charges for each ion species in the electrolyte, and the ion sizes. In addition, charging at the junction between two oppositely charged membranes mimicking bipolar membranes was explored. High surface charge density leads to large electric fields across the bipolar junction and a compact charge-depletion region.

ACKNOWLEDGMENTS

This work was supported by the Natural Sciences and Engineering Research Council of Canada (NSERC).

REFERENCES

- ¹ J. Vatamanu and D. Bedrov, J. Phys. Chem. Lett. **6**, 3594 (2015).
- ²M. Burgess, J. S. Moore, and J. Rodríguez-López, Acc. Chem. Res. 49, 2649 (2016).
- ³ J. P. Valleau, R. Ivkov, and G. M. Torrie, J. Chem. Phys. 95, 520 (1991).
- ⁴D. F. Evans and H. Wennerstrom, *The Colloidal Domain: Where Physics, Chemistry, Biology, and Technology Meet*, 2nd ed. (Wiley, New York, 1999).

- ⁵B. Hou, W. Bu, G. Luo, P. Vanysek, and M. L. Schlossman, J. Electrochem. Soc. **162**, H890 (2015).
- ⁶N. Huang, J. Tao, J. Liu, S. Wei, L. Li, and Z. Wu, Soft Matter 10, 4236 (2014).
- ⁷F. Mugele, B. Bera, A. Cavalli, I. Siretanu, A. Maestro, M. Duits, M. Cohen-Stuart, D. Van Den Ende, I. Stocker, and I. Collins, Sci. Rep. 5, 10519 (2015).
- ⁸P. Długołkecki, P. Ogonowski, S. J. Metz, M. Saakes, K. Nijmeijer, and M. Wessling, J. Membrane Sci. **349**, 369 (2010).
- ⁹ A. J. Bard and L. R. Faulkner, *Electrochemical Methods: Fundamentals and Applications*, 2nd ed. (Wiley, New York, 1980).
- ¹⁰M. Z. Bazant, K. Thornton, and A. Ajdari, Phys. Rev. E **70**, 021506 (2004).
- ¹¹V. N. Duradji and D. E. Kaputkin, J. Electrochem. Soc. **163**, E43 (2016).
- ¹²S. W. Lee, Scanning Electrometer for Electrical Double-Layer (SEED): The Direct Measurement of Ion Dynamics for Biosensor (University of Nebraska-Lincoln, 2013)
- ¹³ H. Park, D. Kim, and K. S. Yun, Sens. Actuators, B 150, 167 (2010).
- ¹⁴H. Zhao, Electrophoresis **32**, 2232 (2011).
- ¹⁵H. von Helmholtz, Ann. Phys. Chem. **165**, 211 (1853).
- ¹⁶M. Gouy, J. Phys. Theor. Appl. **9**, 457 (1910).
- ¹⁷D. L. Chapman, Philos. Mag. 25, 475 (1913).
- ¹⁸O. Stern, Z. Elektrochem. **30**, 508 (1924).
- ¹⁹I. Borukhov, D. Andelman, and H. Orland, Phys. Rev. Lett. **79**, 435 (1997).
- ²⁰I. Borukhov, D. Andelman, and H. Orland, Electrochim. Acta 46, 221 (2000).
- ²¹ R. D. Coalson and A. Duncan, J. Chem. Phys. **97**, 5653 (1992).
- ²² J. J. Bikerman, Philos. Mag. **33**, 384 (1942).
- ²³ M. Eigen and M. Wicke, J. Phys. Chem. **58**, 702 (1954).
- ²⁴E. Wicke and M. Eigen, Die Naturwissenschaften **38**, 453 (1951).
- ²⁵E. Wicke and M. Eigen, Z. Elektrochem. **56**, 551 (1952).
- ²⁶P. Strating and F. W. Wiegel, J. Phys. A: Math. Gen. **26**, 3383 (1993).
- ²⁷ P. Strating and F. W. Wiegel, *Physica A* **193**, 413 (1993).
- ²⁸K. Bohinc, V. Kralj-Iglic, and A. Iglic, Electrochim. Acta 46, 3033 (2001).
- ²⁹ K. Bohinc, A. Iglic, T. Slivnik, and V. Kralj-Iglic, Bioelectrochemistry 57, 73 (2002).
- 30 A. A. Kornyshev, J. Phys. Chem. B 111, 5545 (2007).
- ³¹ M. S. Kilic, M. Z. Bazant, and A. Ajdari, Phys. Rev. E 75, 021502 (2007).
- ³² M. S. Kilic, M. Z. Bazant, and A. Ajdari, Phys. Rev. E 75, 021503 (2007).
- ³³ M. Z. Bazant, M. S. Kilic, B. D. Storey, and A. Ajdari, Adv. Colloid Interface Sci. 152, 48 (2009).
- ³⁴ X. Jiang, J. Huang, J. Zhao, B. G. Sumpter, and R. Qiao, Condens. Matter 26, 284109 (2014).
- ³⁵B. Giera, N. Henson, E. M. Kober, M. S. Shell, and T. M. Squires, Langmuir 31, 3553–3562 (2015).
- ³⁶ J. H. Chaudhry, S. D. Bond, and L. N. Olson, J. Sci. Comput. 47, 347 (2011).
- ³⁷J. L. Liu and B. Eisenberg, Phys. Rev. E **92**, 012711 (2015).
- ³⁸ A. A. Yazdi, A. Sadeghi, and M. H. Saidi, J. Colloid Interface Sci. **442**, 8 (2015).
- ³⁹ H. Sugioka, J. Phys. Soc. Jpn. **85**, 124006 (2016).
- ⁴⁰J. Ying and D. Xie, Appl. Math. Model. **58**, 166 (2018).
- ⁴¹ J. Xing and Y. Jian, Meccanica **53**, 135 (2018).
- ⁴²J. López-García, J. Horno, and C. Grosse, Micromachines 9, 647 (2018).
- ⁴³P. B. Peters, R. van Roij, M. Z. Bazant, and P. M. Biesheuvel, Phys. Rev. E **93**, 053108 (2016).
- ⁴⁴L. Jubin, A. Poggioli, A. Siria, and L. Bocquet, Proc. Natl. Acad. Sci. U. S. A. 115, 4063 (2018).
- ⁴⁵K. Jiao and X. Li, Prog. Energy Combust. Sci. 37, 221 (2011).
- ⁴⁶M. Eikerling and A. Kulikovsky, *Polymer Electrolyte Fuel Cells: Physical Principles of Materials and Operation* (CRC Press, 2014).
- ⁴⁷K. Kreuer, S. J. Paddison, E. Spohr, and M. Schuster, Chem. Rev. **104**, 4637 (2004).
- ⁴⁸K. Oguro, N. Fujiwara, K. Asaka, K. Onishi, and S. Sewa, Electroact. Polym. Actuators Devices **3669**, 64 (1999).
- ⁴⁹ N. Fujiwara, K. Asaka, Y. Nishimura, K. Oguro, and E. Torikai, Chem. Mater. 12, 1750 (1999).
- ⁵⁰Z. A. Goodwin, M. Eikerling, H. Löwen, and A. A. Kornyshev, Smart Mater. Struct. 27, 075056 (2018).

- ⁵¹ M. Matse, P. Berg, and M. Eikerling, Phys. Rev. E **98**, 053101 (2018).
- ⁵² M. Matse, P. Berg, and M. Eikerling, Eur. Phys. J.: Spec. Top. **227**, 2559 (2019).
- ⁵³ M. V. Fedorov and A. A. Kornyshev, Chem. Rev. **114**, 2978 (2014).
- ⁵⁴S. Kondrat, O. A. Vasilyev, and A. A. Kornyshev, J. Phys. Chem. Lett. **10**, 4523 (2019).
- 55 A. Levy, J. P. de Souza, and M. Z. Bazant, "Breakdown of electroneutrality in nanopores," arxiv.org/abs/1905.05789.
- ⁵⁶W. B. Zimmerman, Multiphysics Modeling with Finite Element Methods (World Scientific Publishing Company, 2006), Vol. 18.
- ⁵⁷D. Henderson, S. Lamperski, L. Bari Bhuiyan, and J. Wu, J. Chem. Phys. **138**, 144704 (2013).
- ⁵⁸C. Xu, H. Du, B. Li, F. Kang, and Y. Zeng, J. Electrochem. Soc. **156**, A435–A441 (2009).

- ⁵⁹ P. Perret, Z. Khani, T. Brousse, D. Bélanger, and D. Guay, Electrochim. Acta 56, 8122 (2011).
- ⁶⁰ A. L. d'Entremont and L. Pilon, J. Power Sources 273, 196 (2015).
- ⁶¹ J. J. Lado, R. E. Pérez-Roa, J. J. Wouters, M. I. Tejedor-Tejedor, C. Federspill, J. M. Ortiz, and M. A. Anderson, Sep. Purif. Technol. 183, 145 (2017).
- ⁶²M. Kaisti, Biosens. Bioelectron. **98**, 437 (2017).
- ⁶³T. L. Horng, P. H. Tsai, and T. C. Lin, Comput. Math. Biophys. 5, 142 (2017).
- 64 L. J. Cheng and L. Jay Guo, Chem. Soc. Rev. 39, 923 (2010).
- 65 S. Prakash and A. T. Conlisk, Lab Chip 16, 3855 (2016).
- 66 M. Ünlü, J. Zhou, and P. A. Kohl, J. Phys. Chem. C 113, 11416 (2009).
- ⁶⁷ K. N. Grew, J. P. McClure, D. Chu, P. A. Kohl, and J. M. Ahlfield, J. Electrochem. Soc. 163, F1572 (2016).
- ⁶⁸ J. M. Ahlfield, L. Liu, and P. A. Kohl, J. Electrochem. Soc. **164**, F1165 (2017).